Suspended liquid particle disturbance on laser-induced blast wave and low density distribution

Takahiro Ukai*, Hossein Zare-Behtash, Konstantinos Kontis

University of Glasgow, School of Engineering, Glasgow, G12 8QQ, UK

Corresponding author: *Takahiro Ukai

email: *Takahiro.Ukai@glasgow.ac.uk*

Telephone: + 44-141-330-2477

Abstract:

The impurity effect of suspended liquid particles on laser-induced gas breakdown was experimentally investigated in quiescent gas. The focus of this study is the investigation of the influence of the impurities on the shock wave structure as well as the low density distribution. A 532 nm Nd: YAG laser beam with 188 mJ/pulse was focused in the chamber filled with suspended liquid particles 0.9 ± 0.63 μm in diameter. Several shock waves are generated by multiple gas breakdowns along the beam path in the breakdown with particles. Four types of shock wave structures can be observed: 1) the dual blast waves with similar shock radius, 2) the dual blast waves with large shock radius at the lower breakdown, 3) the dual blast waves with large shock radius at the upper breakdown, 4) the triple blast waves. The independent blast waves interact with each other and enhance the shock strength behind the shock front in the lateral direction. The triple blast waves lead to the strongest shock wave in all cases. The shock wave front that propagates towards the opposite laser focal spot impinges on one another, and thereafter a transmitted shock wave (TSW) appears. The TSW interacts with the low density core called a kernel, the kernel then longitudinally expands quickly due to a Richtmyer-Meshkov like instability. Laser-particle interaction causes an increase in the kernel volume which is approximately five times as large as that in gas breakdown without particles. In addition, laser-particles interaction can improve the laser energy efficiency.

Keywords: Laser-induced gas breakdown; Suspended liquid particles; Impurity effect; Hot plume

I. INTRODUCTION

Numerical and experimental investigations have demonstrated that the laser energy addition technique is applicable to aircraft for improvement of their aerodynamic performances. Laser-induced gas breakdown was first observed in 1963 [1-3]. Thereafter, the laser-induced gas breakdown was believed to be applicable to a wide range of engineering applications such as flow control [4-6] and laser plasma igniters [7, 8] to name a few. Flow control using laser-induced gas breakdown has been shown to significantly contribute to drag reduction [9-11] and modification of shock waves [12-15]. Sperber *et al.* [16] demonstrated that a drag reduction of approximately 40% and 60% can be achieved in Mach 2.1 and 2.7, respectively. Furukawa *et al.* [15] applied the laser energy deposition technique to a supersonic free-flight model and suggested that shock wave modification due to laser energy deposition has the potential to mitigate the sonic boom level. Tamba *et al.* [17] and Osuka *et al.* [18] attempted to control shock-boundary layer interaction, which occurs on supersonic/hypersonic vehicles, by repetitive-pulse laser energy deposition and showed that shock-boundary layer interaction can be controlled.

Laser-induced gas breakdown is accompanied by a thermal spot and a blast wave. The thermal spot and the blast wave play a key role in influencing the aerodynamic performances. A local high temperature region corresponding to a low Mach number region induces shock wave movement when the thermal spot interacts ahead of a shock wave. According to both numerical and experimental investigations of laser energy addition ahead of a bow shock wave [11, 19, 20], the local high temperature region modifies the shape of the bow shock wave. The local stand-off distance increases in the vicinity of the thermal spot because of the relative low Mach number at the thermal spot. Thereafter, a vortex ring is generated due to baroclinic effects and remains on a blunt body surface for a period. The vortex ring is associated with a drag reduction [21, 22], and the residence time of the vortex ring is proportional to the drag reduction [23]. Moreover, what is important is that the drag reduction has a linear dependence on the thermal spot size as well as the ratio between the model surface area interacting with the thermal spot and the thermal spot size. According to a numerical investigation of the effect of laser energy deposition on a normal shock-boundary layer interaction in a viscous duct flow [12], a blast wave induced by gas breakdown enhances the wall pressure behind the separation point where the normal shock wave occurs. This pressure enhancement increases the flow separation region, which is the length between the flow separation and reattachment points. However, lower energy addition hardly influences the flow characteristics. The strength of the blast wave and thermal spot size are the important parameter to provide sufficient effectiveness of laser energy deposition.

The local thermal structure induced by the gas breakdown alters when the laser beam is focused in any kind of impurities. The optical system for laser focusing greatly affects the laser discharge [24, 25]. Spherical aberration of the lens, the unfocused beam diameter, and the lens focal length all influence the laser intensity profile along the beam path in the vicinity of the ideal focal spot [24]. The breakdown threshold significantly depends on gas-medium, gas pressure, and the laser wavelength [26, 27]. In a pure gas, a long wavelength as well as a high medium pressure decrease the breakdown threshold [28, 29]. The breakdown threshold in aerosols or any impurities shows the same tendency as that in a pure gas; however, it is generally lower than the theoretical predictions and experimental results [30-32]. Pinnick *et al.* [31] investigated effects of aerosols on breakdown thresholds at various laser wavelengths and showed that breakdown thresholds are 2 to 3 orders of magnitude below those for pure air. The breakdown threshold for a 10.6 μm laser beam continues to decrease with increasing dust particle size at a range of approximately 0.1 to 100 μm [32, 33]. These results show that the lower breakdown threshold is caused by laser-particle interaction. According to the review article from Lushnikov *et al.* [34], the particle temperature is increased due to laser absorption, and thereafter a higher temperature causes melting and evaporation of the particle. The particle shape may also change due to laser absorption. Moreover, the laser energy absorption efficiency depends on the laser wavelength, particle diameter, and particle temperature. Thus it is expected that the medium gas/particle temperature distribution differs from a local thermal spot induced by gas breakdown in a pure gas because of the higher number of parameters involved when particles are present. The different thermal spot size and structure would affect the blast wave formation because rapid heating is associated with blast waves.

Although previous investigations have shown that the laser-induced gas breakdown technique has benefits for drag reduction and the control of shock wave structures, the importance of impurity effects on the gas breakdown must be recognized before application to aircraft. This is because the laser beam is not necessarily focused in a pure gas without impurities. Therefore, the effect of liquid impurities on laser-induced gas breakdown is experimentally investigated in this study. Since the thermal spot as well as the shock wave structure that is induced by gas breakdown are important factors for flow control, the focus of this study is the investigation of the influences of impurities on the shock wave structure as well as the low density region related to the thermal spot.

II. EXPERIMENTAL SETUP

A laser beam was focused in a quadrilateral stainless steel vacuum chamber with a volume of 0.138 m^3. The chamber has a top quartz window of 98 mm in diameter, and a pair of side quartz windows 137 mm in diameter. The chamber was connected to a vacuum pump, and nitrogen gas was supplied

until the pressure within the chamber recorded 100 kPa after evacuating the air to P_v = 20 kPa. Based on Dalton's law [35], the gas molecule consists of oxygen and nitrogen of approximately 4.2% and 95.8% in the chamber, respectively. Note that it is assumed that the atmospheric gas constituent is oxygen at 21% and nitrogen at 79% in the chamber before evacuating the air. In the present experiments, the pressure and the temperature in the chamber were P_0 = 99.6 ± 0.3 kPa and T_0 = 293.3 ± 1.8 K, respectively. The nitrogen gas was passed through a particle generator (TSI, model: 9307-6, 1000 L/min of aerosol flow rate) to provide oleic acid based oil particles of 0.9 ± 0.63 μm in diameter [36]. The supplied gas pressure was maintained at approximately 150 kPa. The volume of input nitrogen gas is calculated using equation; $V_{in} = (M \cdot R \cdot T_0)/(P_0 - P_v)$, M and R are mass of nitrogen gas and the gas constant, respectively. The mixture of nitrogen gas with suspended particles was supplied into the chamber. According to an experimental result from Echols et al. [37], the Laskin nozzle, which is installed into the particle generator we used, supplies particle mass concentration C_m ≈ 4884 mg/m^3 in the present experimental condition. Therefore, particles with a total mass of m_t = $C_m \cdot V_{in}$ = 150 mg corresponding to 1 ×10^{-3} mg/cm^3 are suspended in the chamber. When considering laser-induced gas breakdown without liquid impurity effects, the nitrogen gas was directly supplied to the chamber. A pressure transducer (Kulite, model: XTE-190M, pressure range: 0 to 170 kPa Absolute) driven by a DC power supply (TAim-TTi, model: EX752M) and k-type thermocouple were installed on the chamber. These signals were monitored using a data acquisition system (National Instruments Corp., model: NI-9205 for pressure monitoring and NI-9213 for temperature monitoring) driven by LabVIEW.

To induce the laser energy focusing in the chamber, a Q-switched pulsed Nd: YAG laser beam with a wavelength of λ = 532 nm was employed. The pulse width is τ_w ≈ 10 ns. A laser grade concave lens with a focal length of -50 mm expands the laser beam and a second laser grade convex lens with a focal length of 150 mm collimates the laser beam. The laser beam then passes through the top window of the chamber. The unfocused collimated beam diameter was approximately D = 25 mm measured using a photographic paper (ILFORD, model: MGIV Multigrade IV RC DELUXE, MGD.1M) before the laser beam passes through the convex lens. The collimated laser beam is focused in the chamber by a laser grade convex lens with a focal length of f = 100 mm which corresponds to a focusing f-number ≡ f / D = 4. The laser energy in the vicinity of the laser focal spot was E_{in} = 188 mJ/pulse measured using a power meter (Coherent Inc., model: PM USB LM-45).

The laser-induced blast wave and a low density core were visualised using high-speed schlieren photography with a standard Z-type optical arrangement. The schlieren system consists of a continuous light source with a 450 W Xe arc lamp (Newport, model: 66921), a condenser lens with a focal length of 70 mm, an iris diaphragm, a pair of 203.3 mm diameter concave mirrors with a focal length of 1829

mm, a knife-edge, an imaging lens, and a high-speed camera either Fastcam SA1.1 (Photron, maximum special resolution: 1024 × 1024 pixels) or HPV-1 (Shimadzu, special resolution: 312 × 260 pixels). The iris in front of the condenser lens creates a light spot that illuminates the first parabolic mirror. The light beam is then collimated by the first mirror and passes through the quartz side window of the test section. A second parabolic mirror reflects the collimated beam after the beam passed through the test section and another quartz side window. The knife-edge is horizontally positioned at the focal point of the second parabolic mirror. The imaging lens in front of the camera focuses the image to the camera sensor. The images were acquired at a frame rate of 37.5 kfps (Fastcam SA1.1) and 500 kfps (HPV-1) with an exposure time of 1 μs. An offset angle between the collimated light beam and the light path from the light source to the first/second mirrors was set at 12 degrees to prevent coma aberration.

III. RESULTS AND DISCUSSIONS

A. Shock wave structure

Different shock wave formation/propagation become apparent in the laser-induced gas breakdown with and without particles. Figure 1 shows the time evolution of schlieren images of the laser induced-gas breakdown without liquid particles. The elapsed time after the breakdown is defined as t [μs]. The laser beam is focused from the top in each image. Rapid local heating due to the laser focusing results in plasma generation, which can be seen as the bright region in the schlieren images. A laser-induced blast wave (LBW) propagates spherically into the surrounding gas. Schlieren images of the typical shock wave structures in laser-induced gas breakdown with particles as well as the schematic of the interaction are shown in Figs. 2 to 5. It seems that several shock waves are generated by multiple breakdowns at the different breakdown locations along the beam path. The reason why multiple breakdowns appear along the beam path will be discussed in the following paragraph. These shock wave structures are categorized into four types; Category 1: the dual breakdowns (Fig. 2), Category 2: the dual breakdowns with large energy consumption at a lower breakdown position (Fig. 3), Category 3: the dual breakdowns with large energy consumption at an upper breakdown position (Fig. 4), Category 4: the triple breakdowns (Fig. 5),

In Category 1, dual breakdowns induced by similar laser energy consumption at two breakdown points leads to two spherical shock waves. The shock wave fronts that propagate towards the opposite breakdown point impinge on one another, and thereafter the transmitted shock waves (TSWs 1 and 2) appear. Since the speed of sound in the heated spot is faster than that in the surrounding gas [38], the TSWs travel through the heated spot faster, which results in a longitudinal elliptic shape in each blast wave. In Category 2, the breakdowns are induced at two locations along the beam path but the laser

160 energy is relatively more consumed at the lower breakdown point. This results in a large shock radius
161 at the lower breakdown point. The shock wave structure in Category 3 is formed in an inverted position
162 of that in Category 2. In other words, the strong shock wave is generated at the upper breakdown point.
163 In Category 4 in which the triple breakdowns can be observed (Fig. 5), a middle breakdown generates
164 LBW 2 that interacts with LBW 1 and LBW 3, and thereafter the LBWs are coalesced at $\Delta t > 4$ μs.
165 The LBWs are transformed to the TSWs when the shock fronts imping on the others. Since the shock
166 radii of the LBWs 1 and 3 are smaller than that of LBW 2 at the elapsed time of 4 μs, the coalesced
167 LBW forms a shuttle shape; however, the shuttle shaped LBW gradually transforms into a spherical
168 shape. It seems that the shock wave strength of the LBWs 1 and 3 is weaker than that of the LBW 2
169 because the high shock Mach number causes a larger shock radius for LBW 2 at the elapsed time of 4
170 μs.

171 The condition of suspended particles leads to the shock wave structures which were categorized
172 here into four types. In dual breakdowns (Category 1), the laser beam impinges on suspended particles
173 above the ideal focal spot, which results in breakdown due to laser-particle interaction. Even when the
174 laser energy is consumed at the location where the first breakdown occurred, the laser energy is still
175 sufficiently high so that another breakdown can be generated. The laser beam is focused towards the
176 ideal focal location thereafter, and the laser power density reaches the breakdown threshold due to the
177 narrow beam waist in the vicinity of the ideal laser focal spot. Even though the power density is lower
178 than the gas breakdown threshold in pure air, the impingement on the suspended particle causes
179 breakdown because the breakdown thresholds are 2 to 3 orders of magnitude below those for pure air
180 [40]. If the laser energy consumption at the upper breakdown location is the same as lower one, the
181 shock wave structure of Category 1 appears. The location of the particles interacting with the laser
182 beam alters the laser energy consumption at each breakdown point. In Category 2, the laser beam
183 impinges on fewer particles at the upper breakdown point, whereas more particles impinge on the
184 upper breakdown point in Category 3 compared with Category 2. Since particles are suspended
185 randomly, the occurrence of the shock wave structures of all Categories is a random event. Although
186 the shock wave structures observed here are categorized into four types, there is a possibility that
187 different shock wave structures can occur in different particle concentrations. Additionally, the laser
188 properties (wavelength and input energy etc.), the environment (gas pressure and gas molecule), and
189 particle properties (material and size) would cause different shock structures because they all influence
190 the breakdown threshold [26, 27, 30-34].

191 The breakdown appears at a lower laser energy density region due to laser-particle interaction.
192 Figure 6 shows the different laser focal locations for gas breakdown with and without particles. A
193 needle, the shadow on the right hand side in the image, is located in the vicinity of the ideal laser focal

spot so that the location of the multiple breakdown points can be detected. The ideal focal position corresponds to the centre of the LBW in gas breakdown without particles. In breakdown with particles, a longer longitudinal bright region related to plasma generation appears, which results in multiple laser-induced blast waves being produced in close proximity to one another (Figs. 2 to 5). Thereafter, a longitudinal elliptic shaped blast wave is formed due to the interaction of the multiple LBWs. As shown in Figs. 2 to 5, the multiple breakdown regions are only generated along the beam path. This allows us to expect that the laser beam with a narrow beam waist impinges on the particles around the ideal laser focal spot. In the breakdown with particles, the centre of the LBW is positioned at z = 2.1 ± 0.2 mm above the ideal laser focal spot. The plasma can also generate at the upper part of the ideal focal spot. A possible scenario is that liquid particles melt due to local heating induced by the impingement of the laser beam with particles, and a vapour plume is formed due to vaporization from particle melting. Because the interaction between the vapour and the laser beam results in ionization of the gas [39], the laser-particle interaction induces a plasma. Based on the breakdown locations, the laser power density is estimated. The laser beam converges and diverges towards the ideal laser focal location. The breakdown without particles appears at the ideal focal spot, and the beam waist r_0 at the ideal focal spot is calculated as [40];

$$r_0 = r(0) = \frac{\lambda \cdot f}{\pi \cdot {}^{D}/_{2}} \tag{1}$$

It is assumed that the laser beam has a Gaussian intensity profile. In the case of suspended particles, the breakdown is generated above the ideal laser focal spot, and the location of the breakdown is sufficiently away from the ideal focal location ($z >> z_R$). Thus the beam radius at which the breakdown appeared is expressed as [41];

$$r(z) \approx \frac{z \cdot \lambda}{\pi \cdot r_0} \qquad (\text{for } z \gg z_R)$$
$$\text{where the Rayleigh range } z_R = \frac{f^2 \cdot \lambda}{\pi \cdot ({}^{D}/_{2})^2} \tag{2}$$

Laser power density Q at the breakdown location is calculated using equation (3).

$$Q = \frac{E_{in}/\tau_w}{\pi \cdot r(z)^2} \tag{3}$$

Laser power densities with and without particle interaction cases are $Q \approx 5.5 \times 10^{11}$ and 3.3×10^{14} W/cm^2, respectively. The power density at which the breakdown appeared due to laser-particle interaction is significantly lower than that of without particle interaction. The laser-particle interaction induces breakdown even at the lower power density region.

B. Shock radii and shock Mach number

The shock radius and the shock Mach number were obtained from the schlieren images. The longitudinal and lateral radii of the shock wave front are shown in Fig. 7. Figure 7 (b) shows the mean value of all Categories of the shock wave structures. The longitudinal and lateral radii R_a and R_b correspond to the opposite direction of the laser beam incidence and perpendicular to the beam path, respectively. These radii are defined as the distance between the centre of the LBW and the outer shell of the shock front (see sketch in Fig. 7). The centre of the LBW is measured from a range of the elapsed time of 4 and 6 μs. This time is the first instant at which we can recognize the shock wave clearly. The error bars of the shock radii in the breakdown with and without particles show the standard deviation from 48 and 24 repetitions, respectively. The linear approximation curves of the shock radius are estimated using the least-squares method. The Mach number of the shock wave fronts are calculated from temporal variations of shock wave radii, assuming pure nitrogen gas in the chamber, the ambient speed of sound is C_0 = 349 m/s. The shock Mach curves are obtained by logarithmic approximation. The superscript "*w*" and "*w/o*" denote gas breakdown with and without particles, respectively.

Shock wave propagation in the lateral direction leads to the overpressure enhancement behind the shock wave front due to multiple gas breakdowns. In gas breakdown without particles, all the shock radii are almost the same. The longitudinal shock Mach number $M_a^{w/o}$ would be the same as the lateral one $M_b^{w/o}$. Although the longitudinal and lateral shock Mach numbers are not completely the same in the present results, the gradient of the approximation curves are similar. In gas breakdown with particles, the longitudinal shock radius R_a^w is larger than R_b^w at the elapsed time of 4 μs because of the elliptic shaped blast wave; however, the longitudinal and lateral shock radii become similar with time. As shown in Figs. 2 to 5, the several shock waves induced by the longitudinal multiple breakdowns constitute the elliptic shaped LBW. The lateral shock Mach number M_b^w is the fastest of all the Mach numbers in both gas breakdown with and without particles. Since the shock Mach number is proportional to the overpressure magnitude of the blast wave [42], the shock wave that propagates towards the lateral direction leads to the large overpressure behind the shock front. As shown in the sketches of Figs 2 to 5, the several shock waves interact with each other; however, the shock interaction behaviour is different between the shock propagation in the longitudinal and the lateral directions. The shock wave that propagates in the longitudinal direction passes through another shock wave, namely the TSW. In contrast, the shock waves that propagate in the lateral direction would be reflected/combined.

The triple breakdowns lead to a strong shock wave due to shock-shock interaction. Figure 8 shows the comparison of the lateral shock Mach numbers in all the Categories. Approximation curves of

Categories 1 to 3 in which dual breakdowns occur are similar, whereas the triple breakdowns (Category 4) generate a faster Mach number. In Category 4, three independent blast waves are induced by gas breakdown at early stage of the gas breakdown development, whereas two independent blast waves appear in Categories 1 to 3. Since the several blast waves interact with each other in Category 4, there is a higher possibility that more complicated shock interaction appears compared with the other Categories. The multiple shock interactions might cause the formation of a strong shock wave.

C. Laser energy efficiency

Laser-particle interaction leads to higher laser energy consumption. Based on the blast wave trajectory, the initial energy release can be theoretically predicted by a self-similarity solution well known as the Taylor-Sedov approach [43]; however, it is not applicable to weak blast waves. In other words, the Taylor-Sedov solution shows good agreement with only strong blast waves such as nuclear explosion [44]. The self-similarity solutions proposed by Sedov [45], Brode [46], and Jones [47], meanwhile, are applicable to the transition regime of an acoustic wave. Gebel *et al.* [48] applied the above three self-similarity solutions to detect the initial energy release of a weak blast wave and showed that both Brode's and Jones's methods successfully predict the initial energy release. Thus we apply the following Jones's method which is a semi-empirical approach [47] to estimate the initial amount of energy release;

$$\tau = a\left[\left(1 + b \cdot \varepsilon(t)^{\frac{n+2}{n}}\right)^{\frac{2}{n+2}} - 1\right] \tag{4}$$

$$\varepsilon(t) = \frac{R_{pre}(t)}{R_0} \tag{5}$$

$$R_0 = \left[\left(\frac{n+2}{2}\right)^2 \cdot \frac{E_{bw}}{B \cdot \gamma \cdot P_0}\right]^{1/n} \tag{6}$$

$$t = \frac{(\tau \cdot R_0)}{C_0} \tag{7}$$

where τ is the non-dimensional time, a, b, and n are 0.543, 4.61, and 3 for a spherical blast wave respectively. $R_{pre}(t)$ and R_0 are shock radius from the theoretical prediction and a reference radius, respectively. The geometry parameter B, which is deduced by Jones [49], is 5.33 for the specific-heat ratio γ = 1.4. t is the arrival time at the position $R_{pre}(t)$. The blast wave energy E_{bw} that is consumed from the laser energy to generate the blast wave is estimated with an in-house program. The increment of the iterations is 0.1 mJ, and the minimum RMSE (Root Mean Squared Error) leads to the best fitting curve shown in Fig. 9. The RMSE is calculated as;

$$RMSE = \sqrt{\frac{1}{N}\sum_{i=N}^{N}\left(R_{exp}(t)_i - R_{pre}(t)_i\right)^2} \quad (8)$$

where $N = 13$ is the sampling number of the total measured experimental shock radius. R_{exp} is the experimental shock radius. It is assumed that the volume of the elliptic shaped blast wave corresponds to that of a circular blast wave, thus the experimental shock radius can be calculated as: $R_{exp}(t) \sim (R_b(t)^2 \cdot R_a(t))^{1/3}$. The RMSE of the fitting curves for $R_{exp}^{w/o}$ and R_{exp}^{w} are 0.126 and 0.172, respectively. The best fitting curve allows to detect the blast wave energy E_{bw}. The laser energy efficiency $\eta = E_{bw}/E_{in}$ in gas breakdown with and without particles is shown in Table 1. The blast wave energy in breakdown with particles is 2.8 times higher than that without particles; hence, laser-particles interaction can improve laser energy efficiency in creating a blast wave. Note that the present experimental results show that E_{bw} in gas breakdown without particles has a relatively lower laser energy efficiency compared with previous investigations [48, 50] because an optical comportments and the parameters of the laser beam such as input laser energy, laser absorption coefficient, and the focusing *f*-number etc. all influence the laser energy efficiency [40, 50].

D. Low density distribution

The local thermal spot leads to a special low density form called a kernel. Figures 10 and 11 show the sequential images of typical kernel formation with and without particles. These images are captured using the Photron camera. Figure 11 is categorized as the dual breakdowns (Category 1). In gas breakdown without particles (Fig. 10), the kernel is a lateral elliptic shape at the elapsed time of 27 μs although the kernel is almost the circular in shape at $\Delta t < 27$ μs because the schlieren image captured using Shimadzu camera shows the circular shaped kernel at the time of 10 μs in Fig. 1 (d). Thereafter, the bottom region of the kernel moves towards the opposite direction of the laser beam incidence because of the asymmetric temperature distribution [51].

The local low density spot becomes larger in breakdown with the presence of particles. The extreme high gas temperature due to the laser focusing causes the particles surrounding the laser focal spot to melt, which results in the wide low density field around the laser focal location. This is because the high temperature particle, due to laser energy absorption, heats the surrounding particles. In breakdown with particles (Fig. 11), a longitudinal elliptic shaped kernel is formed because the two independent plasma regions generated along the beam path in Category 1. In a single laser focusing [51-53], a vortex ring, which circulates towards the opposite direction of the laser incidence, is generated due to a pressure gradient. The dual breakdowns in which two vortex rings appear leads to these vortices

interaction (Fig. 11 (b) and (c)). As shown in Fig. 11, the turbulent structure can be observed, which results in gas mixing enhancement. Note that the kernel formation depends on both the breakdown location and the number, thus the low density distribution in the other Categories will be discussed in the next paragraph. According to the experimental results of Glumac *et al.* [54], the local gas temperature rises up to approximately 50,000 K at the laser focal spot of the 532 nm laser beam with 150 mJ/pulse. Thus we can expect that a similar thermal spot may appear in present experiments although the laser energy, laser intensity distribution, and unfocused collimated beam diameter are not the same as Glumac's experiment. Considering temperature in Glumac's experiments, it can deduce that the high temperature has the capability to widely melt the particles surrounding the laser focal spot. As previously discussed in the fourth paragraph, Subsection III A (Shock wave structure), the location of the breakdown moves slightly up from the ideal focal position, thereby the laser beam with a larger beam waist has a much higher probability to interact with the vapour plume caused by particle melting. In other words, a wider plasma region appears compared with gas breakdown without particles. This results in the low density spot having much wider distribution.

The volume of the thermal spot and the number are a key factor for the kernel formation in multiple breakdowns. It is deduced that the shape of the thermal spot would be altered depending on Category of the shock structure. This is because multiple breakdowns appear in suspended particles, thereby there is a higher possibility that the thermal spots interact with each other. The various kernel formations in breakdown with particles are shown in Fig. 12. The dual breakdowns (Category 1) lead to two low density cores with a similar volume along the beam path. Since these low density cores occur close to each other, the gas mixing is enhanced at the interaction region. In the dual breakdowns with large energy consumption at the lower breakdown (Category 2), the two low density cores are formed along the beam path; however, the upper density core is smaller than the lower one. This is because less laser energy is deposited at the upper breakdown compared with that at the lower one, thereby the higher temperature spot is smaller. The upper low density core deforms relatively faster than the lower core. This smaller density core is affected by the shock interaction. The transmitted shock wave (TSW2, see Fig. 3), which propagates from the lower breakdown position, longitudinally extends the upper kernel region due to a Richtmyer-Meshkov like instability. In the dual breakdowns with large energy consumption at an upper breakdown (Category 3), the large kernel is formed at the upper breakdown because of the higher laser energy deposited at this location. Due to the interaction of the transmitted shock wave (TSW1, see Fig. 4), the lower small kernel is extended towards the direction of the beam incidence. The small kernel development due to the shock interaction was not necessarily be observed in both Categories 2 and 3. Even when the shock structure is categorized as either Category 2 or 3, the present results show that the small kernel extension is hardly observed. The

reason for this is that the small kernel might be combined with the large kernel when the dual breakdowns occur and the location of the breakdowns is too close. In the triple breakdowns (Category 4), three low density cores are formed and interact with each other. The lower and upper density cores are extended due to the Richtmyer-Meshkov like instability. The transmitted shock waves (TSWs 1 and 3, see Fig. 5), meanwhile, impinge at both upper and lower parts of the middle density core, this in turn causes the collapsed shape of the middle density core.

The vortex motion and instability at the upper/lower kernel region in the multiple breakdowns is due to a pressure gradient induced by the shock interaction. According to an experimental investigation of laser energy deposition at a single focal point [55], the plasma quickly expands and propagates towards the opposite direction of the beam incidence at an early stage of the plasma development, i.e., the high gas temperature spot related to the plasma moves towards the direction of the laser beam source. This results in the teardrop-shaped temperature distribution with a large volume as well as a higher temperature at the focal lens side. The initial temperature distribution generates the blast wave which propagates outward, and a local rapid temperature rise causes a strong blast wave. This results in an expansion wave that produces a pressure gradient towards the centre of the blast wave [56] because the outward shock motion induces an overexpansion of the inner gas [51]. In the multiple breakdowns (Category 2) for example, the temperature distribution induces a vortex ring at the upper kernel region, and thereafter the TSW2 interacts with the kernel corresponding to lighter fluid than the surrounding gas. Since shock propagation is faster in the heated spot (kernel), the faster velocity behind the TSW2 would induce the moving of the surrounding gas into the upper kernel (arrows in Fig. 3). This enhances vortex motion and leads to instability. According to Hawley et al. [57], the inclined interface between the lighter and heavy gases induces the instability of a vortex layer, hence the instability would appear in present experiment because the contact surface of different density is complicated.

Breakdown with particles in which multiple low density cores appear leads to a large volume of the kernel. Figure 13 shows time history of the kernel formation, x and y are defined as the longitudinal and lateral lengths shown in Fig. 10 (d), respectively. These lengths were measured from the schlieren images captured using the Shimadzu camera. The error bars of the lengths in the breakdown with and without particles show the standard deviation from 48 and 24 repetitions, respectively. Both x^{wo} and x^{w} gradually increase with time but x^{w} is longer than $x^{w/o}$ because the wide plasma region generates in the breakdown with particles. Both $y^{w/o}$ and y^{w} have the same tendency of the longitudinal length decreasing then increasing slightly. It is expected that the time range between 40 and 50 μs is a transition region where the growth direction of the longitudinal length changes. In gas breakdown without particles, both $x^{w/o}$ and $y^{w/o}$ have a narrow standard deviation, whereas a larger standard

deviation appears in gas breakdown with particles. In particular, the longitudinal length y^w has a higher standard deviation because both the laser focal location and the number of breakdowns alter greatly along the longitudinal direction; hence, they strongly influence the longitudinal length.

Based on the longitudinal and lateral radii of the kernel $r_x = x/2$ and $r_y = y/2$, the volume rate of the kernel $V_{rate} = V_{pk}^{w}/V_{pk}^{w/o}$ is calculated (Fig. 14). It is assumed that the kernel has an elliptic shape at the elapsed time between 12 and 45 μs, thus its volume can be calculated as: $V_{pk} = {}^{4}/_{3} \cdot \pi \cdot r_x^2 \cdot r_y$. The error bars of volume rate σ_{rate} are estimated using the following equation;

$$\sigma_{rate} = \sqrt{\left(\frac{\partial f}{\partial r_x^{w/o}} \cdot \sigma_x^{w/o}\right)^2 + \left(\frac{\partial f}{\partial r_y^{w/o}} \cdot \sigma_y^{w/o}\right)^2 + \left(\frac{\partial f}{\partial r_x^{w}} \cdot \sigma_x^{w}\right)^2 + \left(\frac{\partial f}{\partial r_y^{w}} \cdot \sigma_y^{w}\right)^2} \tag{9}$$

where the volume rate is a function of $r_x^{w/o}$, $r_y^{w/o}$, r_x^w, and r_y^w. The subscripts "x" and "y" denote the lateral and longitudinal directions, respectively. The standard deviation σ is obtained based on the radii of the kernel. The mean value shows that the low density region in the breakdown with particles is in the range of 4 and 5.5 times as large as that without particles.

IV. CONCLUSION

The impurity effect of suspended liquid particles on laser-induced gas breakdown was experimentally investigated in quiescent gas. Laser-induced gas breakdown was generated in an environmental chamber filled with nitrogen gas with suspended oleic acid based oil particles 0.9 ± 0.63 μm in diameter. To induce the laser energy deposition, a Q-switched pulsed 532 nm Nd: YAG laser beam with an output energy of 188 mJ/pulse was focused in the chamber.

The schlieren images showed that different shock wave formation/propagation are present in laser-induced gas breakdown with and without particles. Several shock waves were generated by multiple breakdowns along the laser beam path. A possible scenario is that the liquid particles melt due to the local heating induced by the impingement of the laser beam on the particles, thereby the laser-particle interaction induces a plasma even at the low power density region.

The shock wave structures are categorized into four types; Category 1: dual breakdowns, Category 2: dual breakdowns with large energy consumption at the lower breakdown, Category 3: dual breakdowns with large energy consumption at the upper breakdown, Category 4: triple breakdowns.

The triple breakdowns in which three independent blast shock waves interact with each other enhanced the shock wave strength behind the shock front in the lateral direction. The shock wave fronts that propagate towards the opposite breakdown position impinged on one another, and thereafter a

transmitted shock wave (TSW) appeared. The TSW interacted with the low density core called the kernel. The kernel then expanded due to a Richtmyer-Meshkov like instability; however, the kernel formation depended on the breakdown location and the number of breakdowns. Laser-particle interaction caused the increase in the kernel volume, and the volume of the kernel in the breakdown with particles was approximately five times as large as that in the gas breakdown without particles. In addition, laser-particles interaction can improve laser energy efficiency in generating a blast wave since the blast energy was 2.8 times higher than in gas breakdown without particles.

Acknowledgments

We would like to dedicate this paper to Prof. Margaret Lucas at The University of Glasgow for her kind arrangement of the usage of the high speed camera and to Dr. Richard Green at The University of Glasgow for setting up the laser facility. This research work was supported by European Commission, H2020-MSCA-IF (Project reference: 654318). The laser facility was supplied by the National Wind Tunnel Facility project (EPSRC grant number: EP/L024888/1).

References

[1] E.K. Damon, R.G. Tomlinson, "Observation of ionization of gases by a ruby laser," *Appl. Opt.* 2, pp.546-547 (1963).

[2] R.G. Meyerand, A.F. Haught, "Gas breakdown at optical frequencies," *Phys. Rev. Lett.* 11 (9), pp.401-403 (1963).

[3] P.D. Maker, R.W. Terhune, C.M. Savage, "Optical third harmonic generation," Proceedings of the 3rd International Congress on Quantum electronics, Paris, Columbia University Press, New York Vol. 2 (1964).

[4] D. Knight, "A short review of microwave and laser discharges for supersonic flow control," AL10-02, *Journal Aerospace Lab* 10 (2015).

[5] D. Knight, "Survey of aerodynamic drag reduction at high speed by energy deposition," *J. Propul. Power.* 24 (6), pp.1153-1167 (2008).

[6] P.K. Tretyakov, V.M. Fomin, V.I. Yakovlev, "New principles of control of aerophysical processes research development," *Proc. of the Int. Conf. on the Methods Aerophys. Res.* (Novosibirsk, June 29-July 3, 1996), Part 2, Inst. Theor. and Appl. Mech., Sib. Div., Russ. Acad. of Sci., Novosibirsk, pp.210-220 (1996).

[7] J.A. Syage, E.W. Fournier, R.Rianda, R.B. Cohen, Dynamics of flame propagation using laser-induced spark initiation: Ignition energy measurement," *J. Appl. Phys.* 64, 1499 (1998).

[8] D. Bradley, C.G.W. Sheppard, I.M. Suardjaja, R. Woolley, "Fundamentals of highenergy spark ignition with lasers," *Combust. Flame* 138 (1-2), pp.55–77 (2004).

[9] D. Riggins, H.F. Nelson, E. Johnson, "Blunt-body wave drag reduction using focused energy deposition," *AIAA J.* 37 (4), pp.460-467 (1999).

[10] O.A. Azarova, "Supersonic flow control using combined energy deposition," *Aerospace* 2, pp.118-134 (2015).

[11] J.-H. Kim, A. Matsuda, T. Sakai, A. Sasoh, "Wave drag reduction with acting spike induced by laser-pulse energy deposition," *AIAA J.* 49 (9), pp.2076-2078 (2011).

[12] H. Yan-, D. Knight, R. Kandala, G. Candler, "Effect of a laser pulse on a normal shock," *AIAA J.* 45 (6), pp1270-1280 (2007).

[13] S.O. Macheret, M.N. Shneider, R.B. Miles, "Scramjet inlet control by off-body energy addition: A virtual cowl," *AIAA J.* 42 (11), pp. 2294-2302 (2004).

[14] S.H. Zaidi, M.N. Shneider, R.B. Miles, "Shock-wave mitigation through off-body pulsed energy deposition," *AIAA J.* 42(2), pp.326-331 (2004).

[15] D. Furukawa, Y. Aoki, A. Iwakawa, A. Sasoh, "Moderation of near-field pressure over a

supersonic flight model using laser pulse energy deposition," *Phys. Fluids* 28, 051701 (2016).
[16] D. Sperber, H.-A. Steimer, S. Fasoulas, "Objectives of laser-induced energy deposition for active flow control," *Contrib. Plasma Phys.* 52 (7), pp.636-643 (2012).
[17] T. Tamba, H.S. Pham, T. Shoda, A. Iwakawa, A. Sasoh, "Frequency modulation in shock wave-boundary layer interaction by repetitive-pulse laser energy deposition," *Phys. Fluids* 27, 091704 (2015).
[18] T. Osuka, E. Erdem, N. Hasegawa, R. Majima, T. Tamba, S. Yokota, A. Sasoh, K. Kontis, "Laser energy deposition effectiveness on shock-wave boundary-layer interactions over cylinder-flare combinations," *Phys. Fluids* 26, 096103 (2014).
[19] Y. Kolesnichenko, V. Brovkin, O. Azarova, V. Grudnitsky, V. Lashkov, I. Mashek, "Microwave energy release regimes for drag reduction in supersonic flows," AIAA paper, AIAA-2002-0353 (2002).
[20] A.A. Zheltovodov, E.A. Pimonov, D.D. Knight, "Energy deposition influence on supersonic flow over axisymmetric bodies," AIAA paper 2007-1230 (2007).
[21] Y. Ogino, N. Ohnish, S. Taguchi, K. Sawada, "Baroclinic vortex influence on wave drag reduction induced by pulse energy deposition," *Phys. Fluids* 21, 066102 (2009).
[22] J.-H. Kim, A. Matsuda, A. Sasoh, "Interactions among baroclinically-generated vortex rings in building up an acting spike to a bow shock layer," *Phys. Fluids* 23, 021703 (2011).
[23] A. Sasoh, J.-H. Kim, K. Yamashita, T. Sakai, "Supersonic aerodynamic performance of truncated cones with repetitive laser pulse energy depositions," *Shock Waves* 24, pp.59-67 (2014).
[24] C.G. Morgan, "Laser-induced breakdown of gases," *Rep. Prog. Phys*. 38 pp.621-665 (1975).
[25] G.V. Ostrovskaya, A.N. Zaidel, "Laser spark in gases," *Sov. Phys.-Usp.* 16 (6), pp.834-855 (1974).
[26] A. Sircar, R.K. Dwivedi, R.K. Thareja, "Laser induced breakdown of Ar, N_2 and O_2 gases using 1.064, 0.532, 0.355 and 0.266 μm radiation," *Appl. Phys. B* 63, pp.623-627 (1996).
[27] J.P. Davis, A.L. Smith, C. Giranda, M. Squicciarini, "Laser-induced plasma formation in Xe, Ar, N_2, and O_2 at the first four Nd:YAG harmonics," *Appl. Opt.* 30 (30), pp.4358-4364 (1991).
[28] A.W. Ali, "On laser air breakdown, threshold power and laser generated channel length," ADA1332111, NRL Memorandum Report 5187 (1983).
[29] R.J. Dewhurst, "Comparative data on molecular gas breakdown thresholds in high laser-radiation fields," *J. Phys. D: Appl. Phys* 11, pp.L191-L195 (1978).
[30] P. Chylek, M.A. Jarzembski, V. Srivastava, R.G. Pinnick, "Pressure dependence of the laser-induced breakdown thresholds of gases and droplets," *Appl. Opt.* 29 (15), pp.2303-2306 (1990).
[31] R.G. Pinnick, P. Chylek, M. Jarzembski, E. Creegan, V. Srivastava, Gilbert Fernandez, J.D. Pendleton, A. Biswas, "Aerosol-induced laser breakdown thresholds: wavelength dependence,"

Appl. Opt. 27 (5), pp.987-996 (1988).

[32] D.E. Lencioni, "The effect of dust on 10.6-μm laser-induced air breakdown," *Appl. Phys. Lett.* 23 (12), pp.12-14 (1973).

[33] G.H. Canavan, P.E. Nielsen, "Focal spot size dependence of gas breakdown induced by particulate ionization," *Appl. Phys. Lett.* 22, 409 (1973).

[34] A.A. Lushnikov, A.E. Negin, "Aerosols in strong laser beams," *J. Aerosol Sci.* 24 (6), pp.707-735 (1993).

[35] F.B. Dutton, "Dalton's law of partial pressures," *J. Chem. Educ.* 38 (8), pp. A545 (1961).

[36] P.J. Thomas, K.A. Butefisch, "An investigation of the influence of the size distribution of seeding particles on LDA velocity data in the vicinity of a large velocity gradient," *Phys. Fluids A* 5 (11), pp.2807-2814 (1993).

[37] W.H. Echols, J.A. Young, "Studies of portable air-operated aerosol generators," NRL Report 5929, U.S. Naval Research Laboratory, Washington, D.C. (1963).

[38] G. Layes, G. Jourdan, L. Houas, "Distortion of a spherical gaseous interface accelerated by a plane shock wave," *Phys. Rev. Lett.* 91 (17), 174502 (2003).

[39] D. Bauerle, Laser processing and chemistry, (Springer, New York, 2011), pp. 4-5

[40] S. Musazzi, U. Perini, "Laser-Induced Breakdown Spectroscopy Theory and Applications," Springer Series in Optical Science 182, (2014).

[41] O. Svelto, D.C. Hanna, "Principles of lasers," Fifth edition, Springer New York Dordrecht Heidelberg London (2010).

[42] J.M. Dewey, "Measurement of the Physical Properties of Blast Waves," Shock Wave Science and Technology Reference Library 9, Experimental Methods of Shock Wave Research, pp.53-58 (2016).

[43] G. Taylor, "The formation of a blast wave by a very intense explosion. I. Theoretical discussion," *Proc. R. Soc. Lond. A* 201, pp.159–174 (1950).

[44] G. Taylor, "The formation of a blast wave by a very intense explosion. II. The atomic explosion of 1945," *Proc. R. Soc. Lond. A* 201, pp. 175–186 (1950).

[45] L.I. Sedov, "Similarity and dimensional methods in mechanics," Academic Press Inc., New York and London (1959).

[46] H.L. Brode, "Point source explosion in air," Research report RM-1824-AEC, The RAND Corporation (1956).

[47] D.L. Jones, "Intermediate strength blast wave," *Phys. Fluids* 11 (8), pp. 1664-1667 (1968).

[48] G.C. Gebel, T. Mosbach, W. Meier, M. Aigner, "Laser-induced blast waves in air and their effect on monodisperse droplet chains of ethanol and kerosene," *Shock Waves* 25, pp. 415-429 (2015).

[49] D.L. Jones, “Strong blast waves in spherical, cylindrical, and plane shocks,” *Phys. Fluids* 4, pp. 1183-1184 (1961).

[50] B. Wang, K. Komurasaki, T. Yamaguchi, K. Shimamura, Y. Arakawa, “Energy conversion in a glass-laser-induced blast wave in air,” *J. Appl. Phys.* 108, 124911 (2010).

[51] I.G. Dors, C.G. Parigger, “Computational fluid-dynamic model of laser-induced breakdown in air,” *Appl. Opt.* 42 (30), pp.5978-5985 (2003).

[52] D. Bradley, C.G.W. Sheppard, L.M. Suardjaja, R. Woolley, “Fundamentals of high-energy spark ignition with lasers,” *Combust. Flame* 138, pp.55-77 (2004).

[53] T.A. Spiglanin, A. Mcilroy, E.W. Fournier, R.B. Cohen, J.A. Syage, “Time-resolved imaging of flame kernels: Laser spark ignition of H_2/O_2/Ar mixtures,” *Combust. Flame* 102 (2), pp.310-328 (2004).

[54] N. Glumac, G. Elliott, M. Boguszko, “Temporal and spatial evolution of a laser spark in air,” *AIAA J.* 43 (9), pp.1984-1994 (2005).

[55] Y.-L. Chen, J.W. L. Lewis, and C. Parigger, “Spatial and temporal profiles of pulsed laser-induced air plasma emissions,” *J. Quant. Spectrosc. Radiat. Transfer* 7, pp.9-103 (2000).

[56] D. Bradley, F.K.K. Lung, “Spark ignition and the early stages of turbulent flame propagation,” *Combust. Flame* 69, pp.71-93 (1987).

[57] J.F. Hawley, N.J. Zabusky ,”Vortex paradigm for shock-accelerated density-stratified interfaces,” *Phys. Rev. Lett.* 63 (12), pp.1241-1245 (1989).

Figures

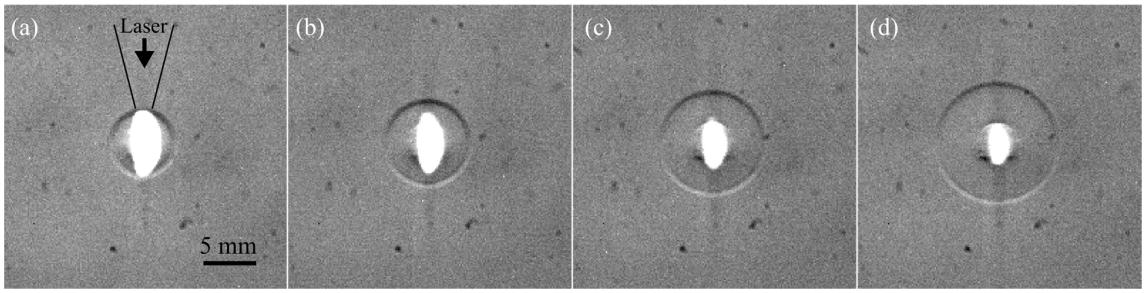

(a) Δt = 4 μs (b) Δt = 6 μs (c) Δt = 8 μs (d) Δt = 10 μs

Figure 1. Typical sequential schlieren images of laser-induced gas breakdown without particles

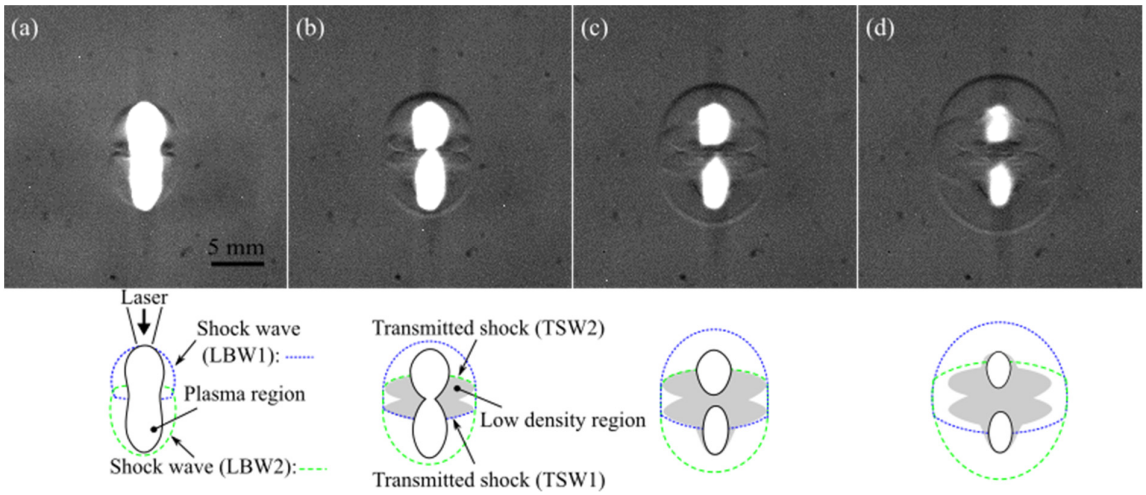

(a) Δt = 4 μs (b) Δt = 6 μs (c) Δt = 8 μs (d) Δt = 10 μs

Figure 2. Laser-induced gas breakdown with particles, Category 1: the dual breakdowns

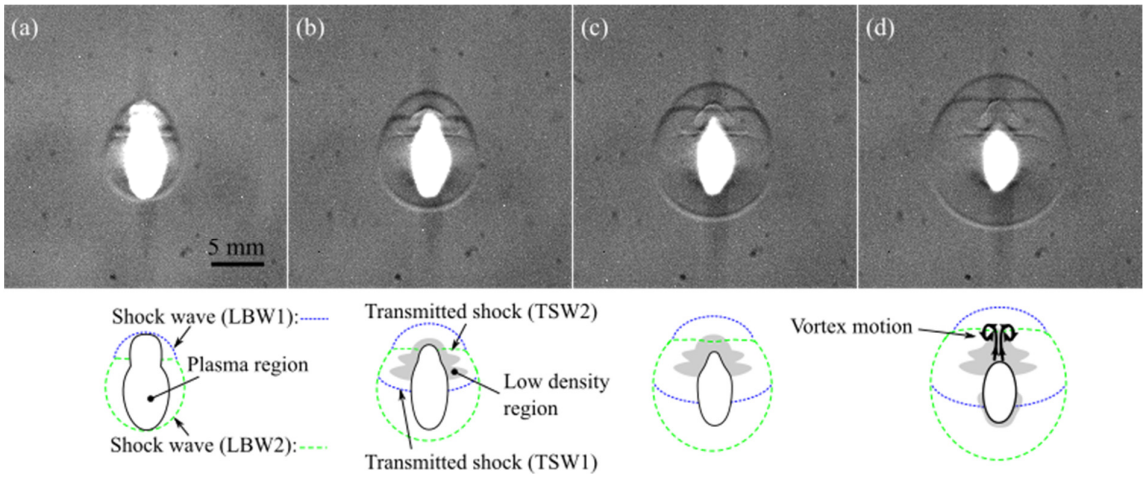

(a) Δt = 4 μs (b) Δt = 6 μs (c) Δt = 8 μs (d) Δt = 10 μs

Figure 3. Laser-induced gas breakdown with particles, Category 2: the dual breakdowns with large energy consumption at the lower breakdown position

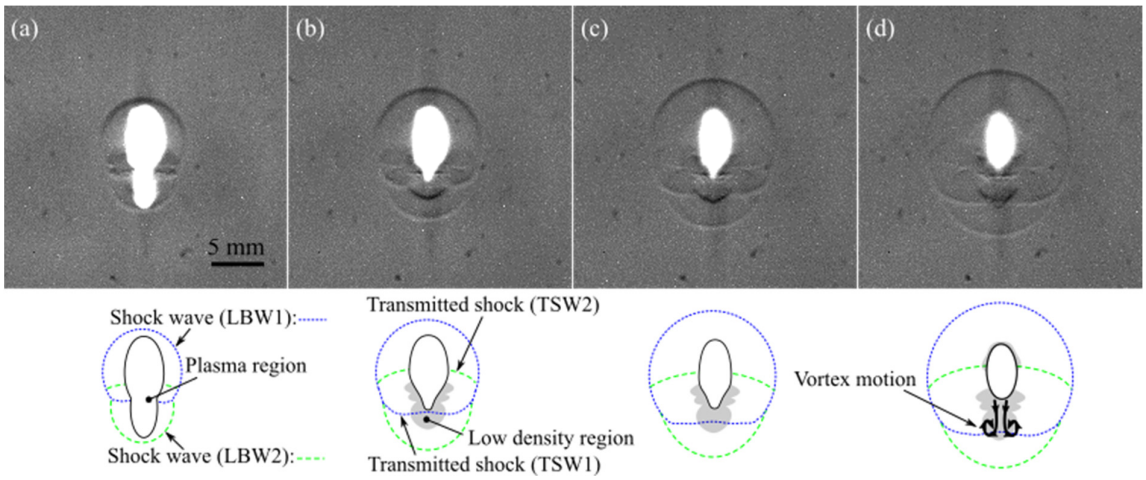

(a) Δt = 4 μs (b) Δt = 6 μs (c) Δt = 8 μs (d) Δt = 10 μs

Figure 4. Laser-induced gas breakdown with particles, Category 3: the dual breakdowns with large energy consumption at the upper breakdown position

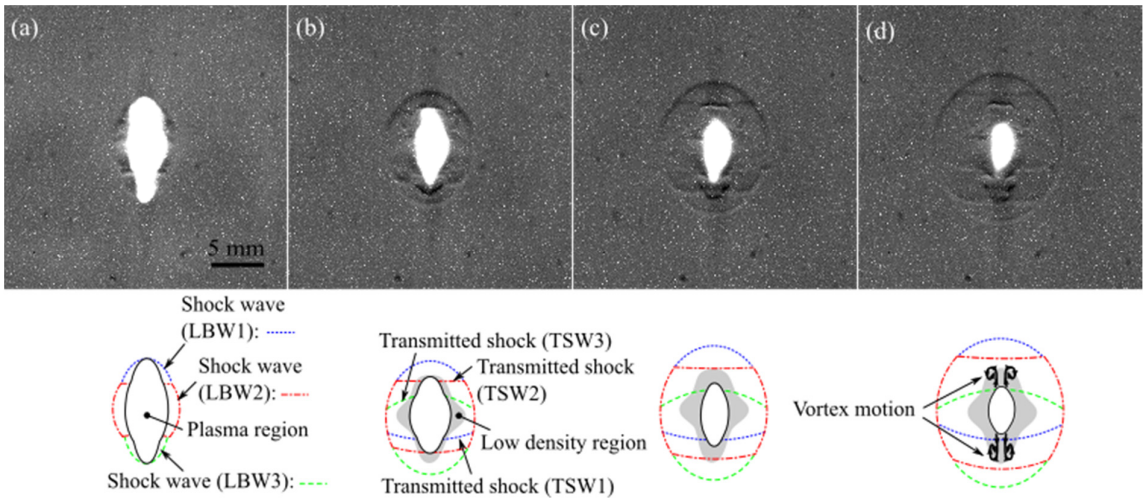

(a) Δt = 4 μs (b) Δt = 6 μs (c) Δt = 8 μs (d) Δt = 10 μs

Figure 5. Laser-induced gas breakdown with particles, Category 4: the triple breakdowns

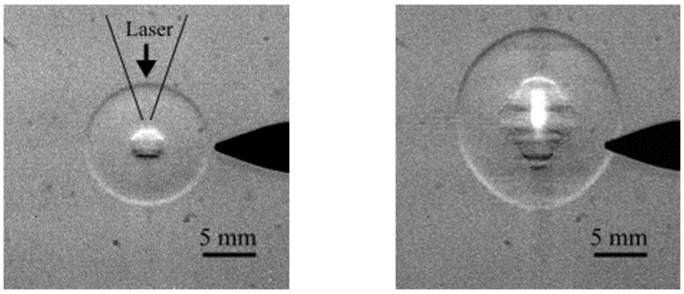

(a) without particles (b) with particles (Category 4)

Figure 6. Typical laser-induced gas breakdown at the elapsed time of 10 μs

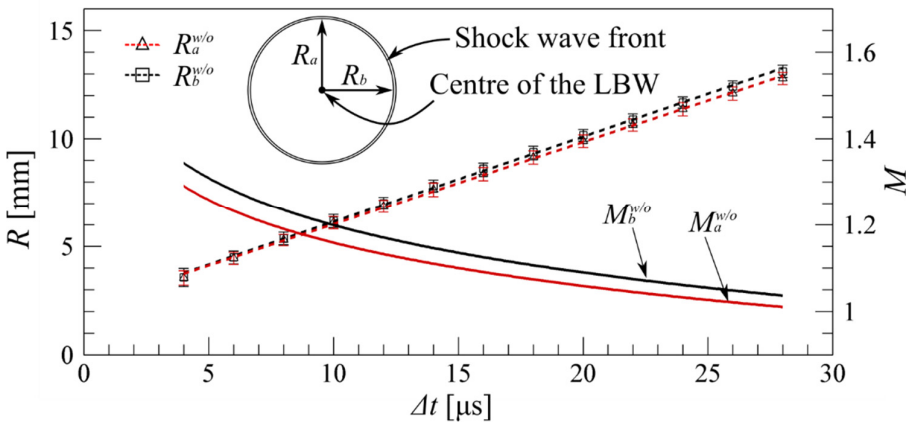

(a) without particles

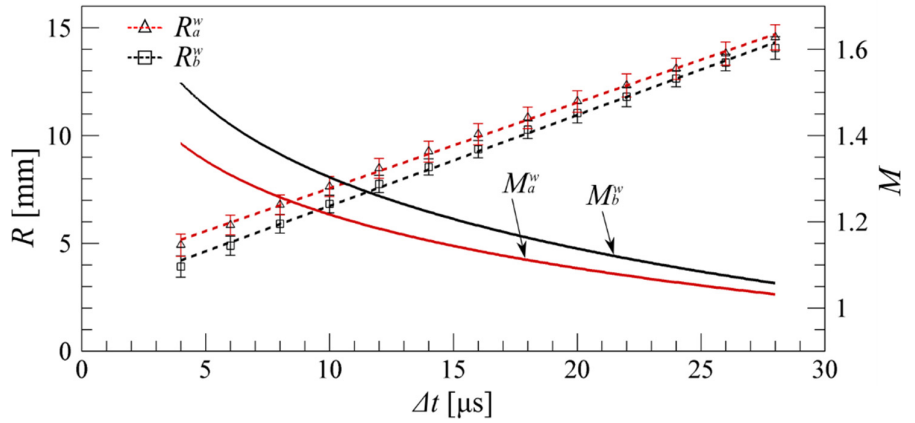

(b) with particles

Figure 7. The longitudinal and lateral radii of the laser-induced blast wave and Mach number of the shock wave front

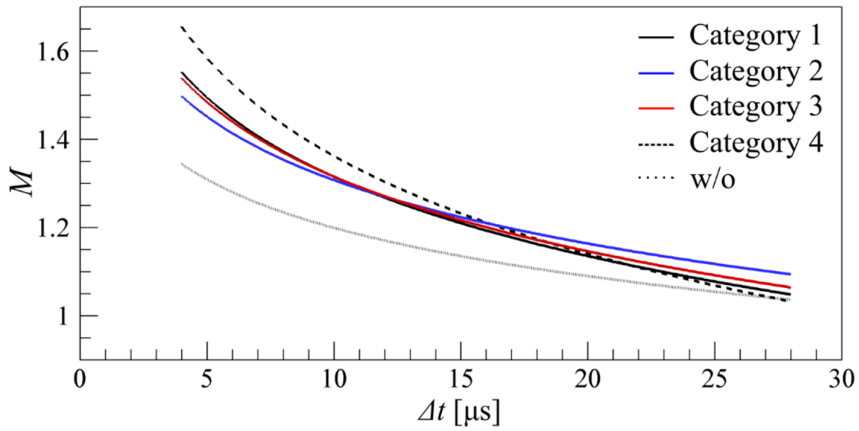

Figure 8. The Mach number of the lateral shock wave front at the various categories, Category 1: the dual breakdowns, Category 2: the dual breakdowns with large energy consumption at a lower breakdown position, Category 3: the dual breakdowns with large energy consumption at an upper breakdown position, Category 4: the triple breakdowns

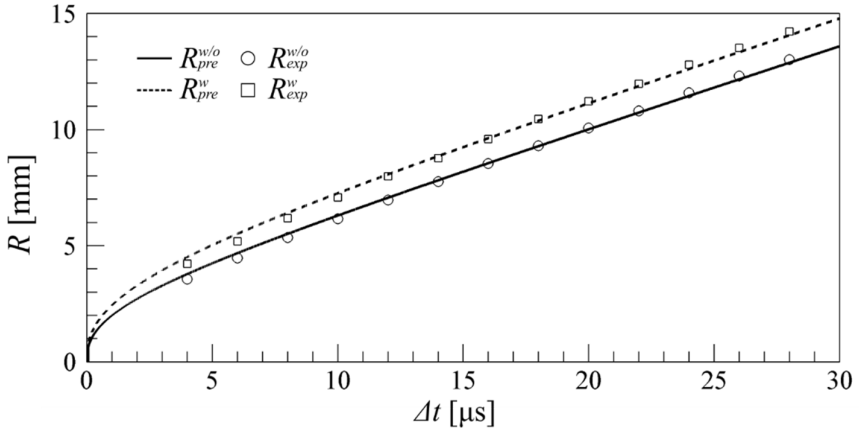

Figure 9. Comparison of the experimental shock radius with the theoretical fitted curve, solid and dashed lines denote the best fitting curve by theoretical predilection method

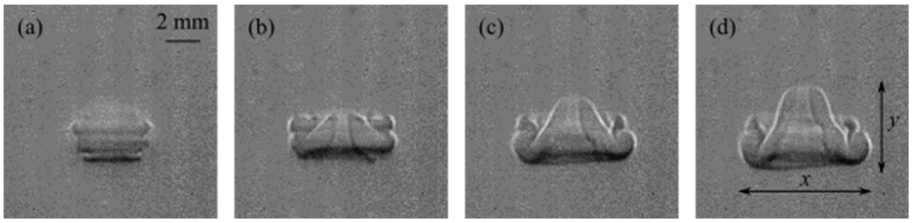

(a) Δt = 27 μs (b) Δt = 108 μs (c) Δt = 189 μs (d) Δt = 270 μs.

Figure 10. Temporal variation of the kernel formation in gas breakdown without particles

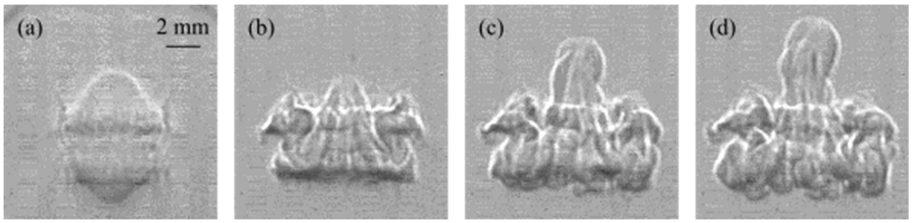

(a) Δt = 27 μs (b) Δt = 108 μs (c) Δt = 189 μs (d) Δt = 270 μs

Figure 11. Temporal variation of the kernel formation in gas breakdown with particles (Category 1)

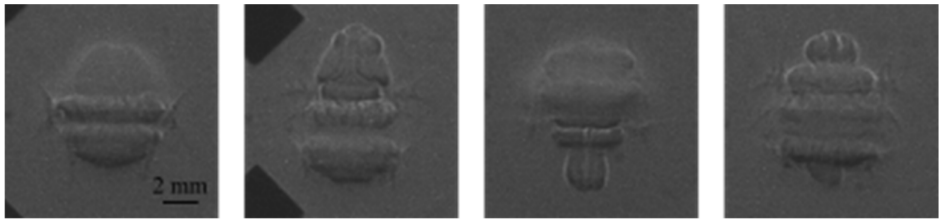

(a) Category 1 (b) Category 2 (c) Category 3 (d) Category 4

Figure 12. Various kernel formations at the elapsed time of 18 μs, Category 1: the dual breakdowns, Category 2: the dual breakdowns with large energy consumption at a lower breakdown position, Category 3: the dual breakdowns with large energy consumption at an upper breakdown position, Category 4: the triple breakdowns

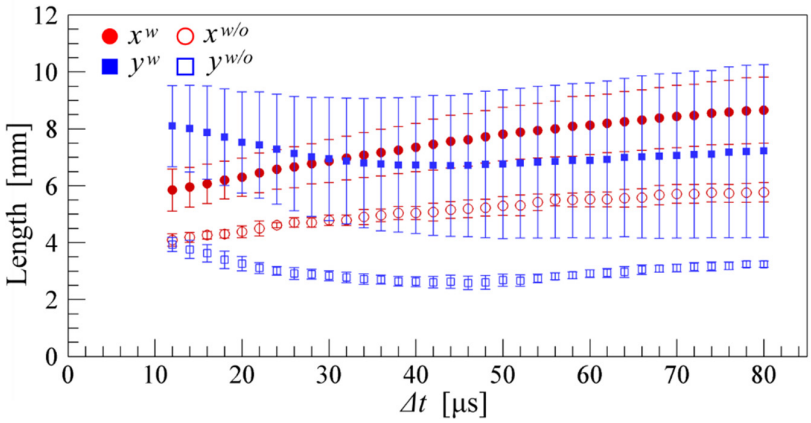

Figure 13. Temporary variation of the longitudinal and lateral lengths of the kernel

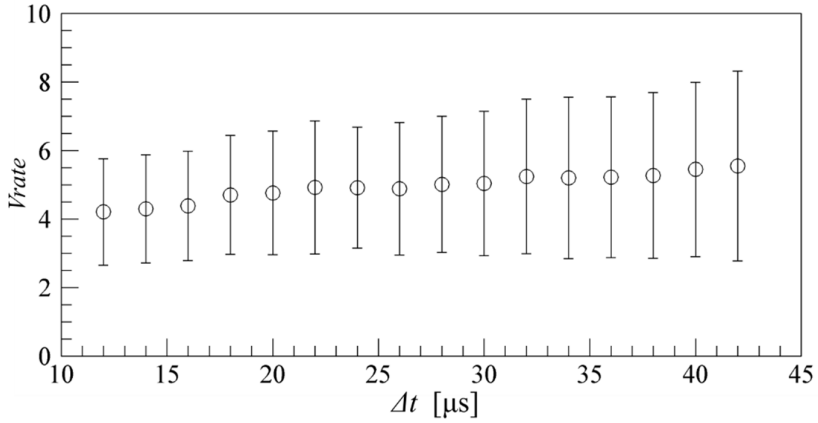

Figure 14. Volume rate of the low density spot

585 **Table**

586 Table 1. Laser energy efficiency in breakdown without and with particles

	Without particles	With particles
$\eta = E_{bw}/E_{in}$ [%]	14	39

587